UC Santa Cruz
UC Santa Cruz Previously Published Works

Title
Application of fluence field modulation to proton computed tomography for proton therapy imaging

Permalink
https://escholarship.org/uc/item/0v24m73z

Journal
Physics in Medicine and Biology, 62(15)

ISSN
0031-9155

Authors
Dedes, G
De Angelis, L
Rit, S
et al.

Publication Date
2017-08-07

DOI
10.1088/1361-6560/aa7734

Peer reviewed

Application of fluence field modulation to proton computed tomography for proton therapy imaging

G. Dedes[1], L. De Angelis[1], S. Rit[2], D. Hansen[3], C. Belka[4], V. Bashkirov[5], R.P. Johnson[6], G. Coutrakon[7], K.E. Schubert[8], R.W. Schulte[5], K. Parodi[1], G. Landry[1]

[1]Department of Medical Physics, Faculty of Physics, Ludwig-Maximilians-Universität München (LMU Munich), 85748 Garching, Germany

[2]Université de Lyon, CREATIS, CNRS UMR5220m Inserm U1044, INSA-Lyon, Université Lyon 1, F69373 Lyon, France

[3]Department of Oncology, Aarhus University Hospital, 8000 Aarhus, Denmark

[4]Department of Radiation Oncology, LMU Munich, 81377 Munich, Germany

[5]Division of Radiation Research, Loma Linda University, Loma Linda, CA 92354, USA

[6]Department of Physics, U.C. Santa Cruz, Santa Cruz, CA 95064, USA

[7]Department of Physics, Northern Illinois University, DeKalb, IL 60115, USA

[8]School of Engineering and Computer Science, Baylor University, Waco, TX 76798, USA

Short title: FMpCT

Number of pages: 29

Number of figures: 14

Number of tables: 4

Corresponding author: Dr. George Dedes, g.dedes@lmu.de

G. Dedes et al. FMpCT

Abstract

This simulation study presents the application of fluence field modulated computed tomography (FFMCT), initially developed for x-ray CT, to proton computed tomography (pCT). By using pencil beam (PB) scanning, fluence modulated pCT (FMpCT) may achieve variable image quality in a pCT image and imaging dose reduction.

Three virtual phantoms, a uniform cylinder and two patients, were studied using Monte Carlo simulations of an ideal list-mode pCT scanner. Regions of interests (ROI) were selected for high image quality and only PBs intercepting them preserved full fluence (FF). Image quality was investigated in terms of accuracy (mean) and noise (standard deviation) of the reconstructed proton relative stopping power (RSP) compared to reference values. Dose calculation accuracy on FMpCT images was evaluated in terms of dose volume histograms (DVH), range difference (RD) for beam-eye-view (BEV) dose profiles and gamma evaluation. Pseudo FMpCT scans were created from broad beam experimental data acquired with a list-mode pCT prototype.

For the virtual phantoms, FMpCT noise in ROIs was equivalent to FF images and accuracy better than -0.7% by using 1% of FF. Integral imaging dose reduction of 37% and 56% was achieved for the two patients for that modulation. Corresponding DVHs from proton dose calculation on FMpCT images agreed to those from reference images and 96% of BEV profiles had RD below 2mm, compared to 1% for uniform low fluence. Gamma pass rates (2%, 2mm) were 98% for FMpCT while for uniform 1%FF they were as low as 59%. Applying FMpCT to preliminary experimental data showed that low noise levels and accuracy could be preserved in a ROI, albeit at lower modulation.

We have shown, using both virtual and experimental pCT scans, that FMpCT is potentially feasible and may allow a means of imaging dose reduction for a pCT scanner operating in PB scanning mode.

1. Introduction

Proton computed tomography (pCT), initially proposed by (Cormack, 1963), has recently seen considerable research interest as a means of reducing range uncertainties in proton therapy (Paganetti, 2012; Yang *et al.*, 2012). By measuring the position and angle of each proton, as suggested by (Huesman *et al.*, 1975), along with the energy loss behind the patient, a relative stopping power to water (RSP) map can be directly reconstructed using dedicated reconstruction algorithms (Penfold *et al.*, 2009; Penfold *et al.*, 2010; Rit *et al.*, 2013; Hansen *et al.*, 2014; Hansen *et al.*, 2016). Recent detector developments coupled with improved computing power have permitted the development and operation of two list-mode pCT scanner prototypes based on broad (passively scattered) proton beam delivery (Hurley *et al.*, 2012; Sadrozinski *et al.*, 2016). The RSP accuracy of pCT is expected to improve the current clinical practice, which is based on the calibration of single energy CT scans with a reported uncertainty of 3.5% (Yang *et al.*, 2012). Additionally, pCT has the potential to equal or outperform the accuracy achievable with dual energy CT (Hünemohr *et al.*, 2013; Hünemohr *et al.*, 2014; Hudobivnik *et al.*, 2016; Mohler *et al.*, 2016), according to the simulation study of (Hansen *et al.*, 2015). Initial results from pCT prototypes operating in list mode suggest at least comparable accuracy to DECT with experimental RSP errors currently below 1.4% for phantoms (Giacometti *et al.*, 2017).

Besides RSP accuracy, pCT benefits from good dose efficiency, yielding better contrast to noise ratio at equivalent dose levels when compared to x-ray CT (Schulte *et al.*, 2005). Early results from pCT prototypes report doses of about 1 mGy to achieve acceptable image quality (Sadrozinski *et al.*, 2016). This is comparable to the imaging dose used by in-room CBCT imaging, and lower than typical x-ray CT treatment planning imaging doses (at least 10 mGy and ranging up 100 mGy, see Table 7 in (Murphy *et al.*, 2007)). A recent DECT publication specific to proton therapy reported doses of 20 mGy (Hudobivnik *et al.*, 2016). This aspect of

pCT suggests the technique could be used for daily low-dose in-room imaging and could compete with x-ray cone-beam CT (CBCT) image quality without the need of corrections, as needed for proton dose calculations on CBCT images (Kurz *et al.*, 2015; Landry *et al.*, 2015a; Landry *et al.*, 2015b; Park *et al.*, 2015; Veiga *et al.*, 2015; Veiga *et al.*, 2016). In x-ray CT, several dose reduction techniques have been developed such as the use of bow-tie filters (Graham *et al.*, 2007b; Mail *et al.*, 2009) and automatic exposure control (Mulkens *et al.*, 2005; McCollough *et al.*, 2006; Kalender *et al.*, 2008). An exciting idea consists of prescribing image quality levels prior to CT scanning using modulation of the x-ray fluence within the fan-beam (Graham *et al.*, 2007a; Bartolac *et al.*, 2011; Bartolac and Jaffray, 2013; Szczykutowicz and Mistretta, 2013a, b). This approach is called fluence field modulated CT (FFMCT) and was recently experimentally realized using the imaging system of a TomoTherapy machine (Szczykutowicz and Mistretta, 2014; Szczykutowicz *et al.*, 2015). The FFMCT concept is very similar to intensity modulated radiation therapy (IMRT) where the mega-voltage photon fluence is modulated with a multi-leaf collimator. The main difficulty with modulating the x-ray fluence of a conventional CT scanner is the lack of an equivalent modulation device. For this reason experimental realization of FFMCT made use of the TomoTherapy machine's imaging system which is equipped with a 64 leaf binary collimator. Another group has achieved FFMCT by using multiple aperture devices (Stayman *et al.*, 2016).

Given the current rise in the number of proton therapy centers equipped with pencil beam scanning (PBS), one can imagine imitating intensity modulated proton therapy (IMPT) instead of IMRT, to create a pencil beam (PB) pCT system allowing fluence modulated pCT (FMpCT). FMpCT would rely on the modulation of the beam intensity during the acquisition of a pCT projection to achieve the desired proton fluence modulation. Using a treatment planning image as guide, an in-room FMpCT scan could thus be acquired with high image quality in the beam path and a lower image quality in regions receiving negligible therapeutic dose levels, leading to a lower

integral imaging dose compared to uniform fluence scans. Such an image could be used for patient positioning, dose recalculation or even re-planning.

The objective of this study was to evaluate the feasibility of FMpCT using a PB pCT Monte Carlo simulation framework and a state-of-the-art pCT reconstruction algorithm. For a simple homogeneous virtual phantom and two patient CT-based virtual phantoms, image quality at different modulation levels was investigated, as well as proton dose calculation accuracy. Furthermore, FMpCT was simulated using broad beam pCT experimental data acquired with a state-of-the-art scanner prototype.

2. Materials and methods

2.1 Proton CT simulation

The simulation platform used in this study is based on Geant4 version 10.01.p02 (Agostinelli *et al.*, 2003) and has been used in previous studies for proton dose calculation in voxelized geometries (Landry *et al.*, 2015b; Schmid *et al.*, 2015; Hudobivnik *et al.*, 2016). The reference physics list QGSP_BIC_HP was used for the simulation of interaction of particles with matter. The simulation platform uses CT images which are converted to mass density and tissue composition using the approach of (Schneider *et al.*, 2000).

Existing list-mode pCT scanner prototypes rely on two tracker modules located up- and down-stream of the scanned object. The tracker modules are made of pairs of two orthogonal silicon strip detectors allowing position and direction detection. A calorimeter, located after the second tracker module, records the residual energy loss. A more detailed description can be found in (Sadrozinski *et al.*, 2016) (see figures 1 and 2 in that publication). In this study, an ideal pCT scanner in the form of two scoring planes, before and after the scanned object (which

is positioned at the origin) was simulated. The two ideal scoring planes composed of the same material as the surrounding world (air), record the exact position, direction and energy of each traversing proton. The planes are positioned perpendicularly to the X axis, which is parallel to the beam, at -15.88 cm and 15.88 cm, both covering a surface of $60 \times 60 cm^2$. This area was chosen for simplicity and does not represent the field of view of a real scanner. The simulated imaging beam consists of a 2D grid of non-divergent proton PBs arranged at 1 cm intervals in the YZ plane. Each PB has a two-dimensional Gaussian proton distribution with σ = 4 mm in air. The Z extent (parallel to the superior inferior patient axis) of the PB grid was adjusted according to each virtual phantom, and the Y extent was set to 25 cm. In order to simulate a tomographic scan, the scanned phantom was rotated around the Z axis at 1° steps, covering an angular span of 360°.

2.2 Virtual phantoms

Three voxelized phantoms were used in this study. The phantoms were derived from x-ray CT scans of IMRT patients. (1) A simple phantom was simulated by overwriting a $1.074 \times 1.074 \times 1 mm^3$ CT image with a 10 cm radius cylinder with 0 HU. Outside the cylinder -1000 HU was used. Note that when using the stoichiometric calibration, 0 HU corresponds to a predefined human tissue composition and not water. For this case a single row of PBs bisecting the cylinder was employed given the Z axis symmetry.

(2) The second phantom was derived from a $1.074 \times 1.074 \times 1 mm^3$ CT scan of a patient (Pat1) treated with IMRT for a brain metastasis with a small planning target volume (PTV) located near the base of the skull. The PTV was 5 cm along the Z axis.

(3) For the third phantom, a $1.074\times1.074\times3mm^3$ CT scan of a paranasal sinus cancer patient (Pat2) was used. The large PTV including lymph nodes was 14.3 cm along the Z axis. For (2) and (3), the PB grid extent in Z was set to cover the PTV plus a margin (see section 2.5).

For each phantom, a 360 projections pCT scan with 10^4 protons per PB per projection was simulated. The corresponding fluence at the first tracker was 9600 protons per cm^2 in a projection. For all simulations the dose to tissue per voxel was scored.

2.3 Fluence modulation

The concept of fluence modulation based on proton PB scans presented in this work relies on the definition of regions of interest (ROIs), in which a high image quality is desirable. The term image quality here refers to RSP noise levels and RSP accuracy. The ROIs should ideally cover the beam path to and include the PTV and could be derived using diagnostic or treatment planning imaging data. Phantom specific ROI generation will be presented below.

A schematic representation of the concept is shown in Figure 1 for a simplified ROI. In this proof of principle study, the PB modulation pattern was obtained by calculating a binary sinogram (PB index vs. projection angle). The sinogram entries were 1 if the central axis of a PB intersects the ROI in a given projection and 0 otherwise. Using this sinogram, the fluence of PBs assigned 0 is reduced by a given fluence modulation factor (FMF), FMF<1, while those PBs assigned 1 preserve full fluence (FF). The modulation was performed as a post-processing step to allow several FMpCT images from a single simulation. When reducing a PB's fluence, list mode data were randomly discarded, ensuring that the energy and spatial distribution of the PBs was preserved.
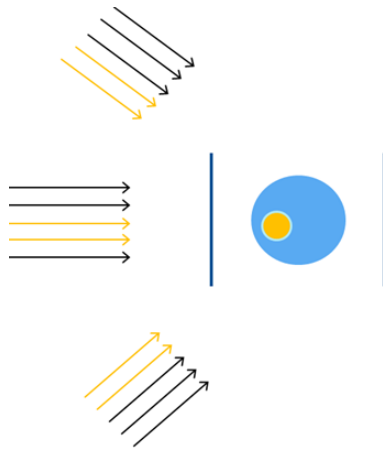
Figure 1. Schematic representation of FMpCT using PBS. PBs whose central axis geometrically intersects the ROI preserve full fluence while the others have their fluence reduced.

2.4 Proton CT reconstruction framework

The reconstruction algorithm chosen for this study was a filtered backprojection (FBP) implementation which accounts for the curved proton paths in the imaged object, mainly due to multiple Coulomb scattering. The main principles of the algorithm are presented in (Rit *et al.*, 2013) and a comparison with different iterative algorithms is presented in (Hansen *et al.*, 2016). The algorithm is based on list mode data, and the actual path of every proton is approximated by a most likely path (MLP) formulation (Schulte *et al.*, 2008), which uses the position and direction information from the scoring planes.

Protons were selected with a 3 standard deviations cut on the energy and angular distributions around their mean energy and angle per projection pixel, in order to filter out nuclear reactions and large angle scattering events, whose energy loss and path cannot be described by the Bethe formula and the MLP formalism. List-mode data were binned in intermediate projection images with 1×1 mm pixels which were then filtered and back-projected. Scans simulated with low fluences can suffer from artefacts due to the absence of proton information in some pixels of the intermediate projections. To counter this, sinogram interpolation (Hansen *et al.*, 2016) was used for all reconstructions. Images were reconstructed

on the same grids as the CT scans used to generate the Geant4 virtual phantoms. For each phantom and each FMF, the following images were reconstructed: (1) a FF image, (2) a FMF·FF uniform fluence image and (3) a FMF FMpCT image.

2.5 FMpCT ROIs and FMF

For the cylindrical phantom, simple circular ROIs with 1 cm radius were studied, as shown in Fig. 2. The FMF was set to 0.1, 0.05 and 0.01. ROI1 was at the center of the cylinder, ROI2 was 37.6 mm off-center and ROI3 was 75.2 mm off-center.

For Pat1 and Pat2, proton treatment plans using PBS were generated for the two patients using a research version of a commercial TPS (Raystation, Raysearch Laboratories, Sweden). For Pat1, a single field uniform dose (SFUD) plan using a 220 degree gantry angle on the International Electrotechnical Commission (IEC) scale was used to deliver 60 Gy to the PTV (15 cm^3). For Pat2, a 3-field IMPT simultaneous integrated boost plan with beams at 0, 100 and 260 degrees was used. The 0 degree field was used only superiorly to the nasal cavities. The high dose PTV (174 cm^3) received 60 Gy and the lymph node PTV (510 cm^3 – 174 cm^3 = 336 cm^3) 50 Gy. For both Pat1 and Pat2, a FMpCT ROI was obtained by using the 10 Gy isodose line, ensuring inclusion of beam paths, PTVs as well as relevant organs at risk. The ROI volumes were 220 cm^3 for Pat1 and 2021 cm^3 for Pat2, and the ROIs are shown in Fig. 3. For Pat1 and Pat2 FMF was set to 0.1, 0.05 and 0.01.
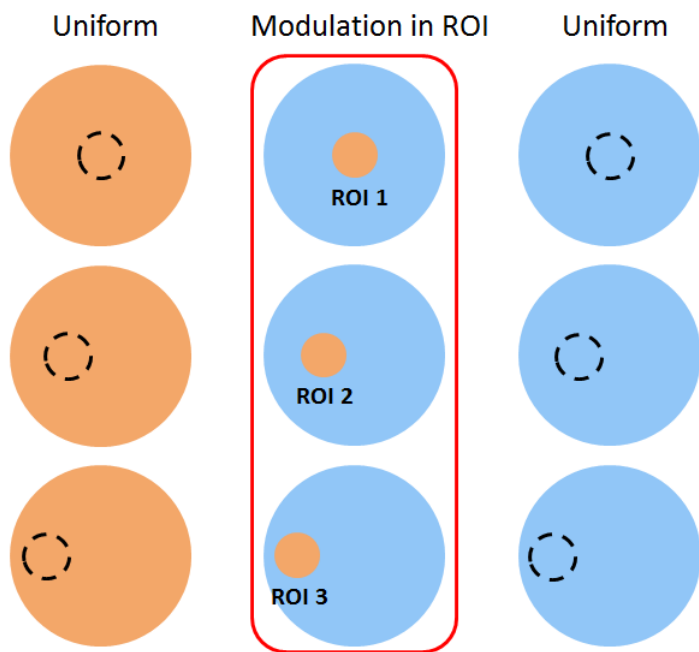
Figure 2. Homogeneous 10 cm radius phantom with three different 1 cm radius ROIs (from top to bottom). The two colors indicate high and low fluence. For each ROI, a uniform FF scan (left), a uniform scan of lower fluence FMF·FF (right), and finally three FMpCT scans of FF inside the ROI and FMF·FF outside (middle) were simulated.
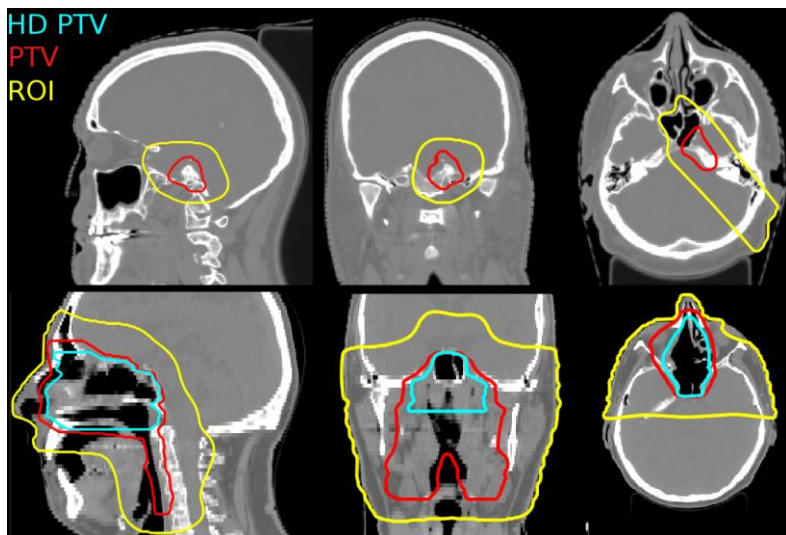

Figure 3. *Top row* Axial, coronal and sagittal slices of the CT image of Pat1, including the FMpCT ROI and PTV. *Bottom row* The same for Pat2, with an additional high dose PTV (HD PTV).

2.6 Image quality

The image quality was quantified according to RSP accuracy and noise. For each virtual phantom a reference RSP distribution was obtained from Geant4 and accuracy was calculated as the mean of $(RSP-RSP_{ref})/RSP_{ref}$ in the FMpCT ROI. Noise was the standard deviation of $(RSP-RSP_{ref})/RSP_{ref}$ in the same ROI. Additionally the imaging dose reduction in the FMpCT images with respect to the FF images, as a function of FMF, was also quantified.

2.7 Dose recalculation

To evaluate dose calculation accuracy on FMpCT images, the reference 3D RSP_{ref} distributions were imported in the TPS with a custom lookup table and used to re-optimize the treatment plans of Pat1 and Pat2. Subsequently, the FF, FMF·FF and FMpCT images were also imported in the TPS and used for plan recalculation. For the SFUD beam of Pat1, beam eye view range (80% of dose maximum) differences to the RSP_{ref} image were computed for dose profiles showing maximum doses higher than 50% of the prescription dose. The percentage of profiles within 1 mm and 2 mm of the RSP_{ref} dose distribution was computed. Additionally, dose volume histograms (DVH) and 2%/2mm gamma pass rates were obtained for the SFUD dose distribution of Pat1 and the IMPT dose distribution of Pat2. For gamma evaluation doses above 50% of the prescription dose were considered.

2.8 Experimental data

In addition to the simulated data, FMpCT was also attempted on experimental data obtained

with the Phase II preclinical prototype pCT scanner (Sadrozinski *et al.*, 2016) of the Loma Linda

University and U.C. Santa Cruz at which a pediatric head phantom (715-HN, CIRS, Norfolk, VA)

was scanned. The 90 projections scan with 2.5×10^6 protons per projections was performed at

the Northwestern Medicine Chicago Proton Center (NMCPC) facility, using a 200 MeV proton

wobbled beam from the IBA universal nozzle for another study (Johnson *et al.*, 2016). The

registered proton fluence per projection in the experimental data was 12000 per cm^2, similar to

that from the simulated data. Although the actual scan was not acquired with fluence modulated

PBs, fluence modulation was emulated during post-processing of the list mode data. For every

proton, a straight line path was constructed from the entrance and exit coordinates provided by

the tracking system of the prototype. The protons whose straight paths did not intersect the

defined ROI were removed from the data with a removal probability of 1-FMF. The goal here was

to assess the impact of FMpCT on image quality compared to the FF image; the general

performance of pCT for this combination of scanner and phantom has been reported elsewhere

(Giacometti *et al.*, 2017). Thus for this part of the study the theoretical RSP in the homogeneous

brain section of the phantom was used as reference and no voxelized ground truth was

employed. Given the lower number of protons in the experimental data (90 projections instead

of 360), higher FMF=0.5, 0.3 and 0.1 were employed. A single cylindrical ROI of 1.5 cm radius
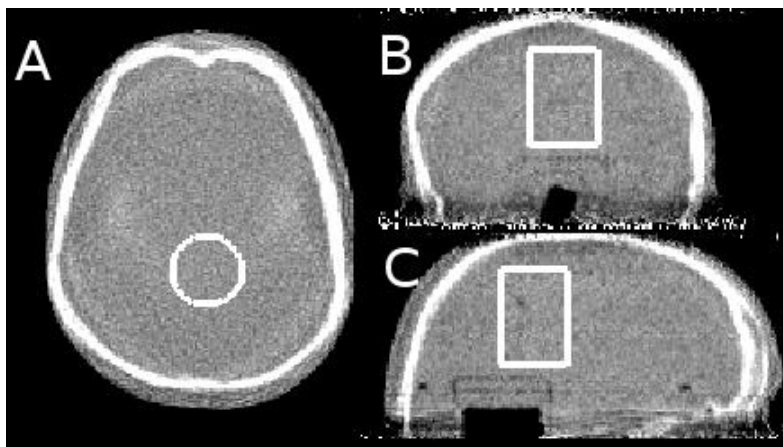
was considered, as shown in Figure 4.

Figure 4. (A) Axial, (B) coronal and (C) sagittal slices of the pCT image of the pediatric head phantom, including the FMpCT ROI in white.

3. Results and discussion

3.1 Uniform phantom

In Figure 5, the reconstructed pCT images of the cylindrical phantom are shown. With increasing FMF, the noise in the images increases as expected. In the case of the FMpCT images, the image quality in the ROIs, indicated by the black circles, was mostly preserved and is summarized in Table 1 in terms of RSP noise and accuracy.
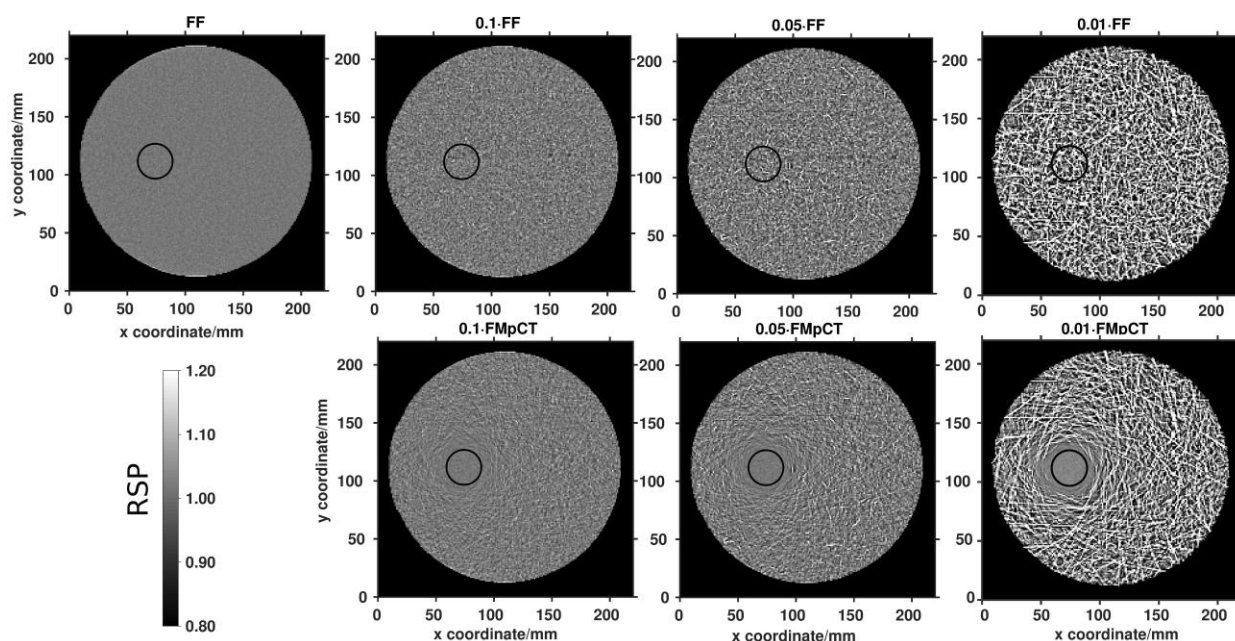
G. Dedes et al. FMpCT

Figure 5. Upper row, left to right: FF image (10^4 protons per PB) and images obtained with homogeneous fluence of 0.1·FF, 0.05·FF and 0.01·FF. Lower row, FMpCT images corresponding to FF in each ROI (black circle) and 0.1·FF, 0.05·FF and 0.01·FF outside. The grayscale corresponds to RSP values.

Table 1. RSP noise (1 standard deviation) and accuracy (mean) results in ROI2. The second column reports RSP noise values for uniform scans with fluence modulation as indicated in the first column. The third column depicts the noise of FMpCT scans. Similarly, the reconstructed RSP mean values in the fourth and fifth columns are given for uniform and FMpCT simulated scans. The reference RSP of the simulated material was 1.02.

Modulation	$(RSP-RSP_{ref})/RSP_{ref}$ (%) noise		$(RSP-RSP_{ref})/RSP_{ref}$ (%) mean	
	Uniform	FMpCT	Uniform	FMpCT
FF	1.2	-	-0.2	-
0.1·FF	4.1	1.2	-0.2	-0.2
0.05·FF	7.0	1.2	-0.3	-0.3
0.01·FF	19.0	1.2	-0.2	-1.3

The results shown in Fig. 5 qualitatively support our hypothesis that FMpCT image reconstruction is feasible when employing the binary fluence modulation scheme presented in Fig. 1. For the three levels of fluence reduction outside ROI2, two distinct image quality levels are seen in each image, as shown in Fig. 5. The image quality metrics reported in Table 1 show that in the case of homogeneous fluence, the noise is approximately inversely proportional to the square root of the proton fluence, while FMpCT reconstruction preserved image quality (both

standard deviation and mean value) down to 5% of the FF. However for FMF=0.01, we observed

a break from the (number of protons)$^{-1/2}$ dependence of the noise as well as a -1.3% shift of the

mean values in the ROI, indicating a limit to the modulation level feasible with FMpCT.

Figure 6 shows an example of the 2D dose distribution in a slice of the homogeneous

phantom, for the case of FF and FMpCT with 0.1·FF for ROI2. Given the nature of the FMpCT

approach, the dose reduction was not uniform throughout the image but was the highest at the

largest distance to the ROI. For the homogeneous fluence imaging case, the dose was uniform

partly due to the fact that the Bragg peak falls outside the object, which means that the protons

traversing it produce a relatively flat dose distribution along their path. This situation is very

different from kV x-ray CT where higher dose is observed at the object's edge due to higher

photon attenuation (Bartolac *et al.*, 2011; Arbor *et al.*, 2015).

Figure 7 shows FMpCT images with 0.1·FF for all three ROIs. The results of the RSP noise

and accuracy analysis as a function of the ROI location were as in Table 1 and did not vary with
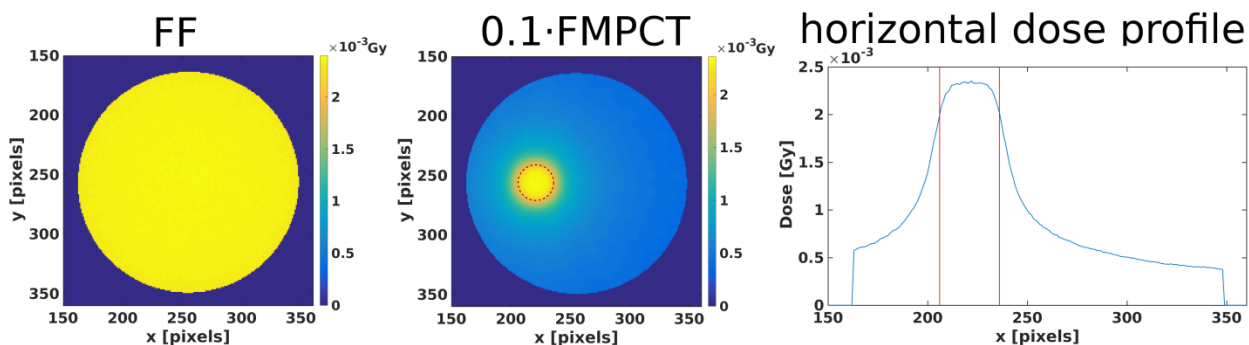
ROI location.

Figure 6. Imaging physical dose distribution in the homogeneous phantom for FF (*left*). Same quantity shown for an FMpCT scan (0.1·FF) for ROI2 (*center*). The imaging integral physical dose was reduced from 2.3 mGy in the FF image to 0.7 mGy in the FMpCT image. (*right)* A dose profile drawn horizontally through ROI2 is shown.

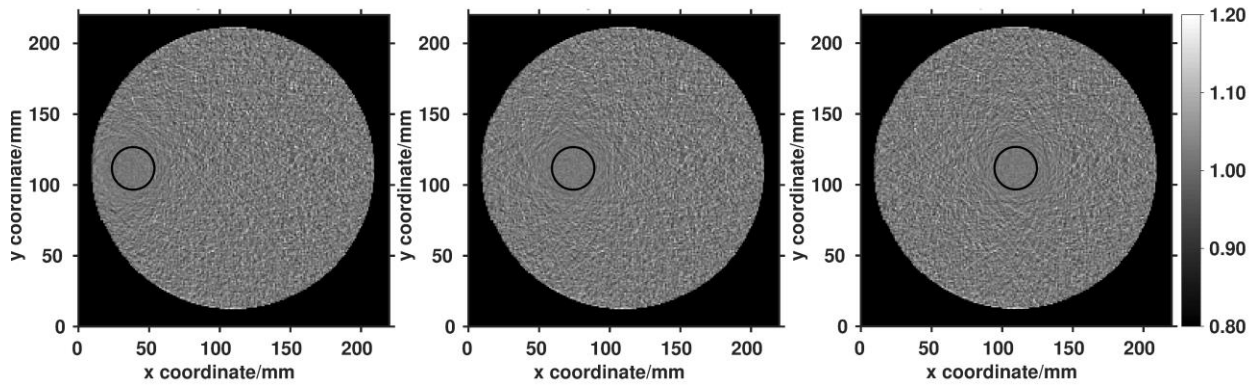**Figure 7**. Three different ROIs defined in the homogeneous phantom, indicated by the black circles, are overlaid on FMpCT images of 0.1·FF.

3.2 SFUD and IMPT cases

Figure 8 shows the uniform FF as well as FMF=0.05 and 0.01 FMpCT for Pat1 where we observed better image quality in the FMpCT ROI used to cover the SFUD beam path. For FMF=0.05, the RSP/RSP$_{ref}$ image is similar in the ROI as the FF image, however for FMF=0.01 slightly lower values were observed (-0.7%, Table 2). Figure 9 presents noise and accuracy as a function of the FMF for Pat1 where we observed that for FMF<0.025 the noise increases more than expected from (number of protons)$^{-1/2}$ and that the accuracy begins to degrade even with FMpCT.
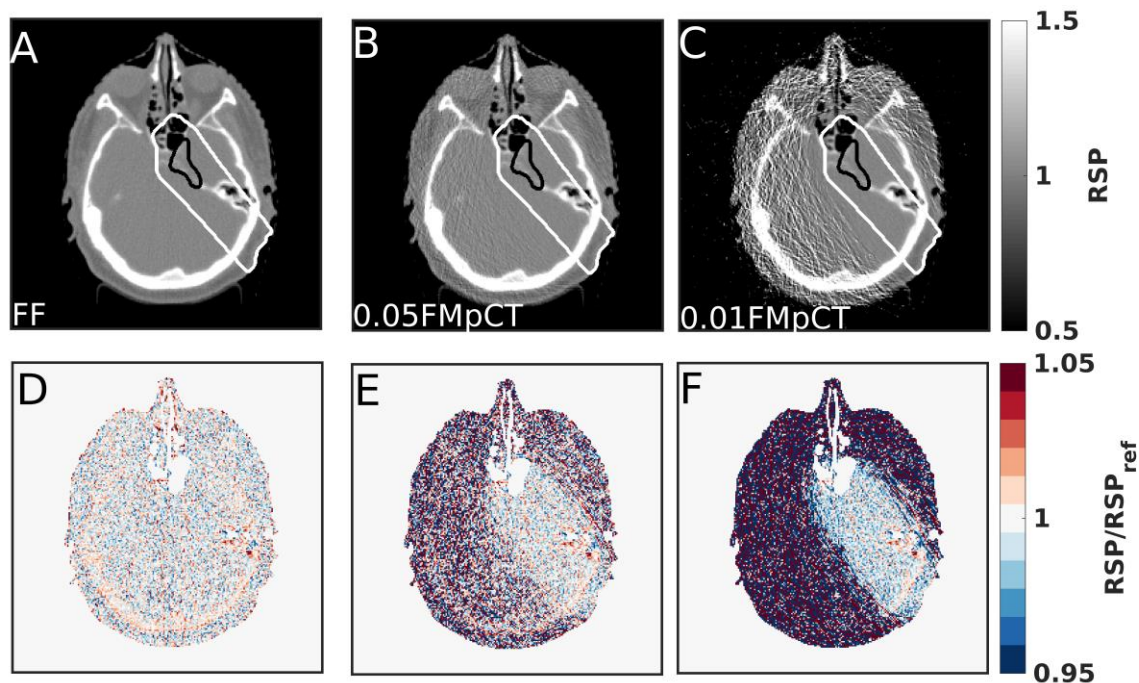
Figure 8. (A) FF pCT image for Pat1. (B) 0.05 and (C) 0.01 FMpCT images. (A-C) the PTV (black) and FMpCT ROI (white) are overlaid on the pCT images. (D-F) Corresponding relative RSP images.
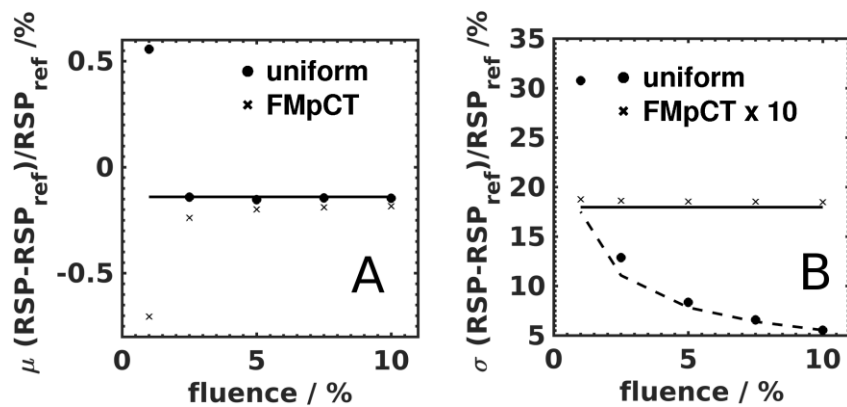

Figure 9. (A) Accuracy (mean, μ) of uniform and FMpCT images for various FMF (expressed as percentage of FF) in the ROI of Pat1. The horizontal solid line corresponds to the FF accuracy. (B) Noise (1 standard deviation, σ) of the same distributions. The FMpCT data are multiplied by 10. The horizontal solid line corresponds to the FF noise and the dashed line to $\sigma_{10\%}(\text{fluence\%}/10\%)^{-1/2}$.

Figure 10 shows the pCT images for Pat2 where similar image quality preservation as Pat1 was obtained from FMpCT. This can be appreciated in Table 2 where the results of the RSP noise and accuracy in the ROIs are tabulated for both patients. The noise levels for Pat1 and Pat2 are

comparable to those from the uniform cylinder (Table 1) at FMF=0.1 and FMF=0.05. At FMF=0.01, the patient images exhibited higher noise. For both Pat1 and Pat2 the FMF=0.01 caused a slightly increased mean error of 0.6 and 0.5% respectively for the uniform fluence, and -0.7 and -0.4% respectively for the FMpCT (visible in Fig.8F and Fig.10F respectively), which is comparable to what was observed with the cylindrical phantom.
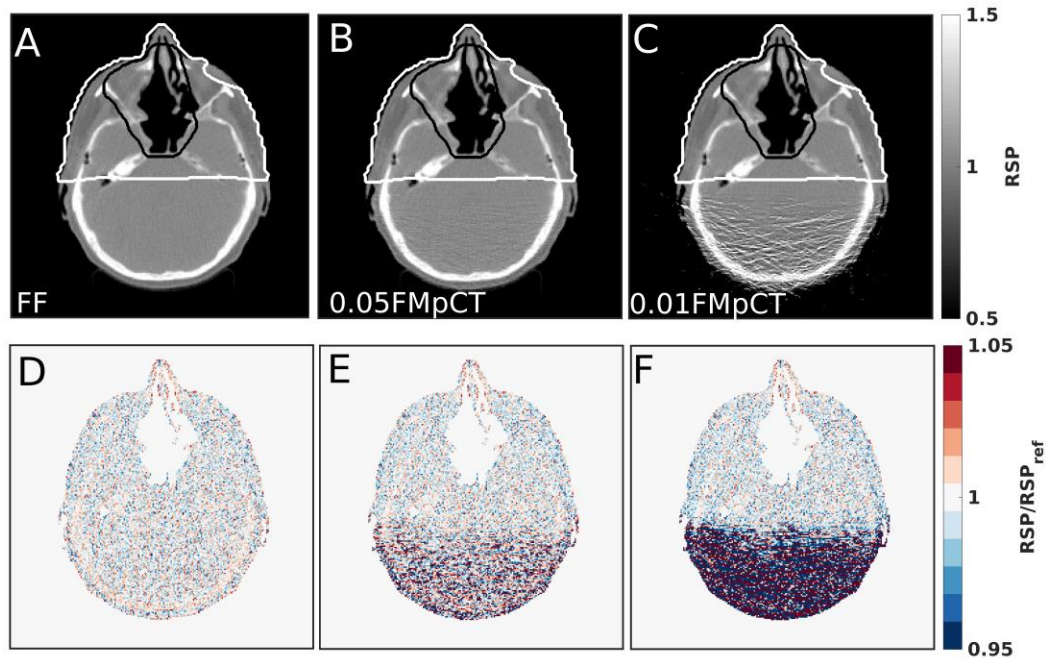

Figure 10. (A) FF pCT image for Pat2. (B) 0.05 and (C) 0.01 FMpCT images. (A-C) the lower dose PTV (black) and FMpCT ROI (white) are overlaid on the pCT images. (D-E) Corresponding relative RSP images.

G. Dedes et al. FMpCT

Table 2. RSP noise (1 standard deviation) and accuracy (mean) results in ROIs for the SFUD (Pat1) and IMPT (Pat2) cases. The second column shows RSP noise values for uniform scans with different FMF. The third column reports noise levels with FMpCT. The fourth and fifth columns refer to the RSP mean reconstructed values in the ROIs for the same imaging configuration.

	$(RSP-RSP_{ref})/ RSP_{ref}$ (%) noise		$(RSP-RSP_{ref})/ RSP_{ref}$ (%) mean	
Pat1	**Uniform**	**FMpCT**	**Uniform**	**FMpCT**
FF	1.8	-	-0.1	-
0.1·FF	5.5	1.8	-0.1	-0.2
0.05·FF	8.3	1.8	-0.2	-0.2
0.01·FF	30.1	1.9	0.6	-0.7
Pat2				
FF	1.4	-	-0.2	-
0.1·FF	4.2	1.5	-0.2	-0.2
0.05·FF	6.3	1.6	-0.2	-0.2
0.01·FF	32.5	1.6	0.5	-0.4

In Figure 11, the imaging dose distributions in the case of uniform FF and FMpCT illustrate the imaging dose reduction achieved for both the SFUD and IMPT cases considered in this study. Table 3 presents the integral doses in the whole image as well as outside the ROIs for both patients. For Pat1 with a small PTV, the integral dose reduction was up to 49% for the whole image and 56% outside the ROI with FMF=0.01. For Pat2, smaller integral dose savings were realized due to the larger PTV and higher number of beams with the same FMF, with a reduction of up to 22% for the whole image and 37% outside the ROI. Interestingly, changing FMF from 0.1 to 0.01 had an effect of less than 5% on integral dose reduction for both cases.

The dose levels reported in this study for the virtual phantoms are based on MC simulation of ideal detectors. Effect such as pileup would contribute to a higher dose compared to our ideal simulation at equivalent image quality. However, the magnitude of the relative dose reduction should not be greatly influenced by the efficiency of real detectors. The lowest possible FMF where image quality is maintained would however probably be higher for realistic detectors.
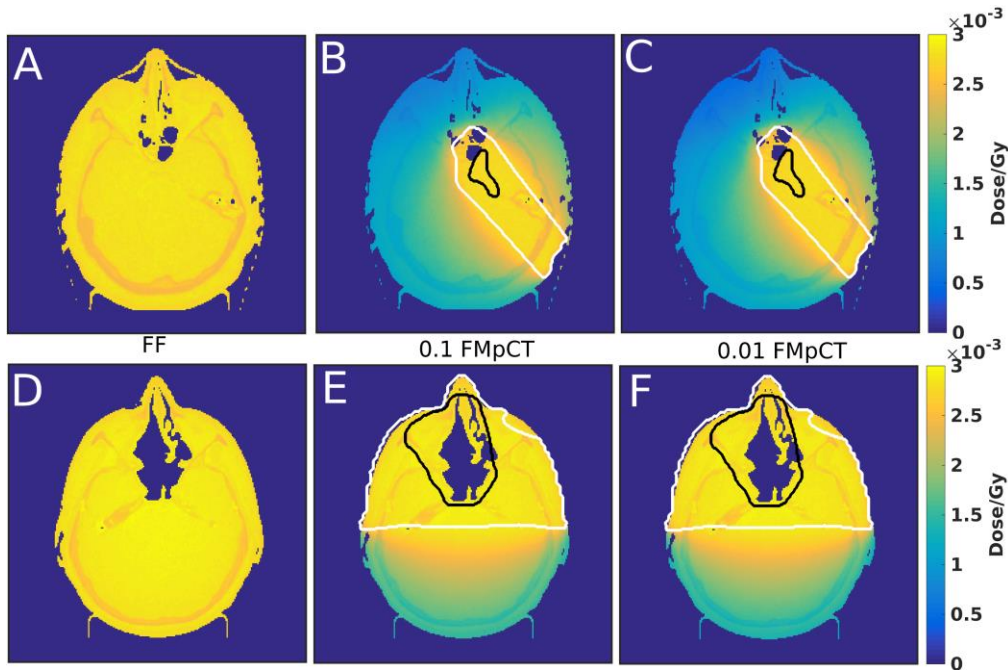
Figure 11. *Top row* Pat1 imaging dose distributions on the (A) FF image, (B) 0.1FMpCT and (C) the 0.01FMpCT image. *Bottom row (*D-F*)* Same for Pat2.

Table 3. Imaging dose in the complete volume and outside the ROI for both patients.

	integral dose (mGy)		integral dose reduction (1-FMpCT/FF)	
Pat1	**whole image**	**outside ROI**	**whole image**	**outside ROI**
FF	2.57	2.56	-	-
0.1·FMpCT	1.42	1.25	0.45	0.51
0.05·FMpCT	1.35	1.18	0.47	0.54
0.01·FMpCT	1.30	1.12	0.49	0.56
Pat2				
FF	2.67	2.65	-	-
0.1·FMpCT	2.13	1.76	0.20	0.34
0.05·FMpCT	2.10	1.71	0.21	0.35
0.01·FMpCT	2.08	1.67	0.22	0.37

In this first attempt at FMpCT, we made use of a simple binary fluence modulation scheme; a more sophisticated fluence optimization approach may yield different spatial dose distributions for equivalent image quality and deserves further investigation. The conformity of the imaging dose to the ROI may be improved by employing continuously varying fluence

modulation profiles and an optimization procedure instead of the binary scheme employed in this proof of principle study. The reason our simple modulation scheme yielded rather acceptable results is attributed to the low attenuation of protons. Indeed, the attenuation of protons traversing 20 cm of water is around 19% for 200 MeV protons and 18% for 300 MeV protons (Quinones *et al.*, 2016). Additionally the inelastic proton cross section is almost independent of the proton energy in the energy range 100-300 MeV. Compared to x-rays, for which 97% of 80 keV photons would be attenuated after 20 cm of water, the calculation of the modulation pattern necessary to obtain the desired image quality is thus more forgiving for FMpCT than FFMCT. Proton dose deposition in the 200-300 MeV range also has a lower material dependency (mass stopping power ratio) than photons in the diagnostic energy range (mass energy absorption coefficient ratio), yielding more homogeneous imaging dose distributions.

The dose calculation accuracy for the SFUD and IMPT treatment plans is presented in Figure 12 for FMF=0.01. We observed that the dose distributions calculated on the FMpCT images agreed with those calculated on the reference RSP_{ref} image in terms of isodose levels and DVH curves. This was not the case for the uniform FMF=0.01 image where dose calculation accuracy was degraded as shown on the DVH of Fig. 12. This was confirmed by the (2%, 2mm) gamma index analysis presented in Table 4. For FMF=0.05 the DVH curves of uniform fluence and FMpCT were identical to the reference.

For the SFUD beam of Pat1, 96% of BEV dose profiles had range differences lower than 2 mm vs RSP_{ref} for FMF=0.01 FMpCT, while with the uniform FMF=0.01 pCT only 1% of profiles passed this test. While the FMF=0.05 FMpCT results compared to RSP_{ref} show limited range agreement improvement compared to uniform fluence (90% vs 87% respectively), when compared to the FF case a clear improvement was seen (99% vs 88% respectively). This result indicates that at this modulation level (FMF=0.05), FMpCT retains better agreement with the FF

G. Dedes et al. FMpCT

image than the uniform FMF=0.05 image. The worst pass rate for FMpCT was 66% of profiles

with range differences of less than 1mm when comparing FMF=0.01 and RSP$_{ref}$. However when

comparing the same FMpCT image to the FF image, the pass rate rose to 97%, indicating that

the lower pass rate was caused by a combination of sub-mm FMpCT errors compared to FF, and

sub-mm systematic FF errors compared to RSP$_{ref}$. The range analysis was found to be sensitive

to the air cavity abutting the PTV (see Fig. 8A) which caused small range shifts in tissue to be

expanded in air. We verified that the 93% pass rate of FF pCT vs RSP$_{ref}$ was caused by beam
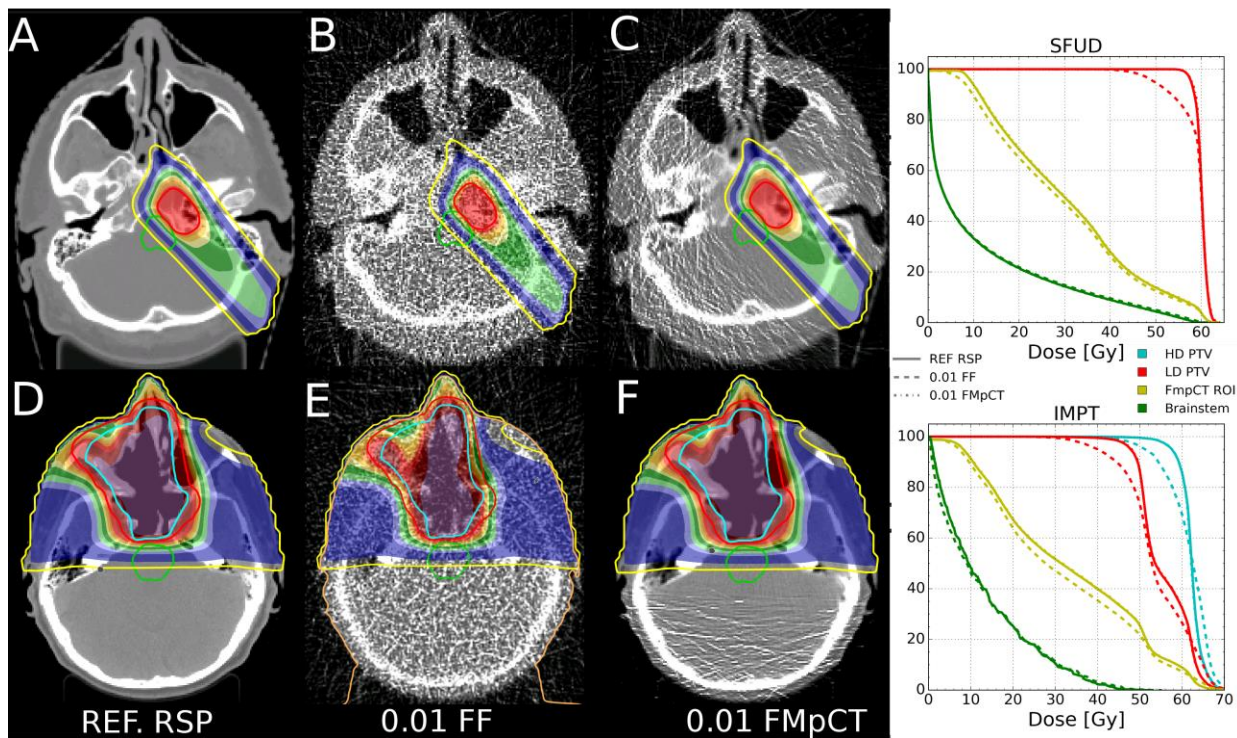
profiles ending in the air cavity.

Figure 12. *Top row* Pat 1 SFUD dose calculation on the (A) SPR$_{ref}$ image, (B) 0.01FF image and (C) the 0.01FMpCT image. *Bottom row* Pat 2 IMPT dose calculation on the (E) SPR$_{ref}$ image, (E) 0.01FF image and (F) the 0.01FMpCT image. The corresponding DVHs are shown on the right.

We have found very little published literature on the impact of CT noise on proton therapy

dose calculation, with one report stating that discontinuities in the CT number to RSP lookup

table might introduce range shifts in the presence of stochastic noise (Brousmiche *et al.*, 2015).

G. Dedes et al. FMpCT

This is not the case for proton CT which has a linear lookup table (Arbor *et al.*, 2015). High levels of noise on CT images can additionally cause a spread of the range at which protons stop, the width of which (4 standard deviations) can reach a few percent of the range at 5.0% CT number noise (Chvetsov and Paige, 2010).

Table 4. SFUD BEV range difference for Pat1. The percentage of profiles with range differences (RDs) below 1 mm and 2 mm are shown. RD are reported using the dose distribution calculated on the RSP_{ref} image and the FF image as reference. For Pat1 and Pat2 the percentage of voxels passing the (2%, 2mm) gamma evaluation is also reported.

Pat1	RD<1mm(%)		RD<2mm(%)		Pat1		Pat2	
						Gamma (2%, 2mm)		
	Uniform	FMpCT	Uniform	FMpCT	Uniform	FMpCT	Uniform	FMpCT
FF – RSP_{ref}	93	-	99	-	99	-	99	-
0.05·FF – RSP_{ref}	87	90	99	99	99	99	99	99
0.01·FF – RSP_{ref}	0	66	1	96	90	98	59	99
0.05·FF – FF	88	99	99	99	-	-	-	-
0.01·FF – FF	0	97	0	99	-	-	-	-

The results of applying FMpCT to broad beam pCT scans of the pediatric head phantom are shown in Figure 13 for the three FMF investigated. We observed a similar trend of reduced accuracy at lower FMF, however this happened at higher FMF for the experimental data. The noise and accuracy are reported in Figure 14, where we observed that FMpCT with FMF below 0.3 showed accuracy degradation larger than 1% as well as increasing noise in the ROI. This appears consistent with the factor 4 lower fluence in the experimental data caused by using 90 projections instead of 360. Thus the experimental FMF=0.3 threshold corresponds approximately to FMF=0.075 from the simulated data. The higher threshold for the experimental data when accounting for the lower number of projections may be explained by the contribution of electronic noise to the projections, which was not modelled in the simulations. A follow up study

making use of the simulation framework presented in (Giacometti *et al.*, 2017) would help clarify these points.

In (Giacometti *et al.*, 2017) the theoretical RSP for the brain material of the pediatric phantom is reported as 1.047; the mean value in the ROI of the FF pCT image was 1.04±0.03, -0.67% lower than the reference. Please note that the theoretical RSP may differ from that measured in a proton beam due to uncertainties on the material composition.

The presented investigation was based on the use of 1cm (FWHM) proton PBs. This value is a realistic estimation of the PB size available at clinical facilities and at PB scanning mode. The current prototype scanner has been used with PB of minimum size of 4cm (FWHM). Due to pileup in the tracker, the maximum counting rate for a PB size of 1cm is approximately 200 kHz. For Pat1 this would mean about 9 seconds per projection at full fluence, resulting into a total scan time of 13.5 min for 90 projections or 54 min for 360 projections. For realistic scan duration, the electronics of the Phase II prototype would have to be modified. The current electronics were designed according to a conservative approach and assuming only scattered proton beams. Therefore an upgrading to faster electronics is not considered a technical obstacle and significantly faster electronics have been already developed and used in other pCT prototypes (Taylor *et al.*, 2016). To achieve a pCT scan with 1cm PBs, without any hardware modification to the scanner, a reduction of the beam intensity will be required. It is still to be investigated whether that can still allow for a dynamic range necessary for FMpCT studies. Alternatively, a more sophisticated fluence modulation technique than the binary intersection pattern could compensate for the larger PB size. A detailed study of the fluence modulation parameters and the detector effect is under way and, we think, beyond the scope of this proof of principle investigation.

Although initially explored in the context of pCT with advanced detectors tracking individual protons, the method could also be applicable to integrating detectors such as range telescopes (Krah *et al.*, 2015; Farace *et al.*, 2016) or using two dimensional detectors (Lee *et al.*, 2015; Tanaka *et al.*, 2016) being also under development. Moreover, the same concept could be extended to imaging with other ions such as ^{4}He and ^{12}C (Shinoda *et al.*, 2006; Hansen *et al.*, 2014; Rinaldi *et al.*, 2014).
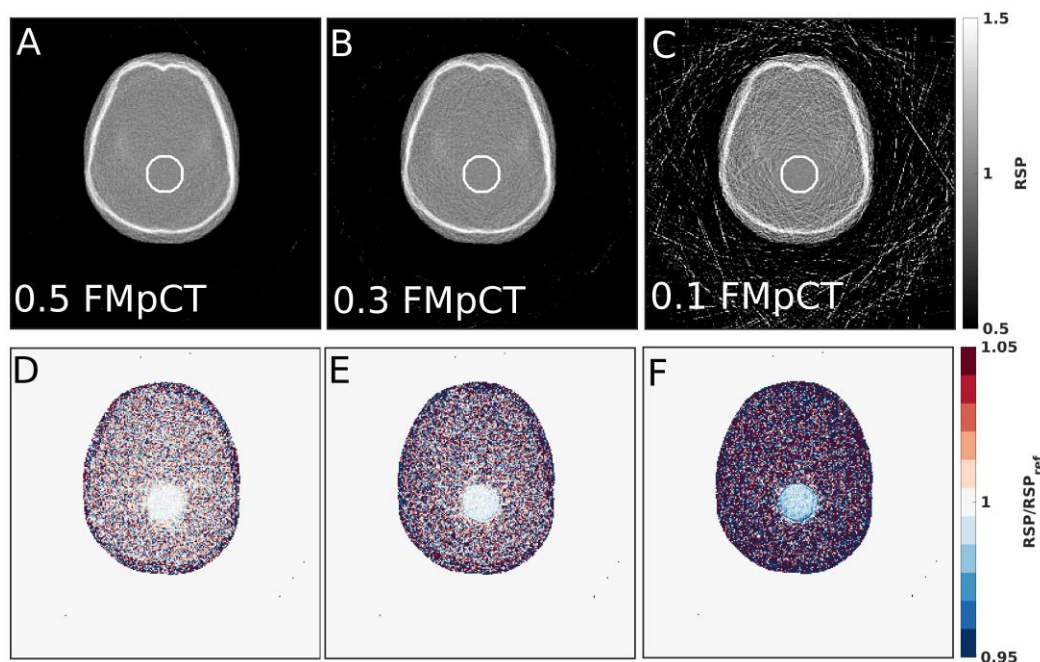
Figure 13. (A) 0.5 (B) 0.3 and (C) 0.1 FMpCT image for the pediatric head phantom. (A-C) The FMpCT ROI (white) used for modulation and analysis is overlaid on the pCT images. (D-E) Corresponding relative RSP images. In this case RSP$_{ref}$ is the FF image.
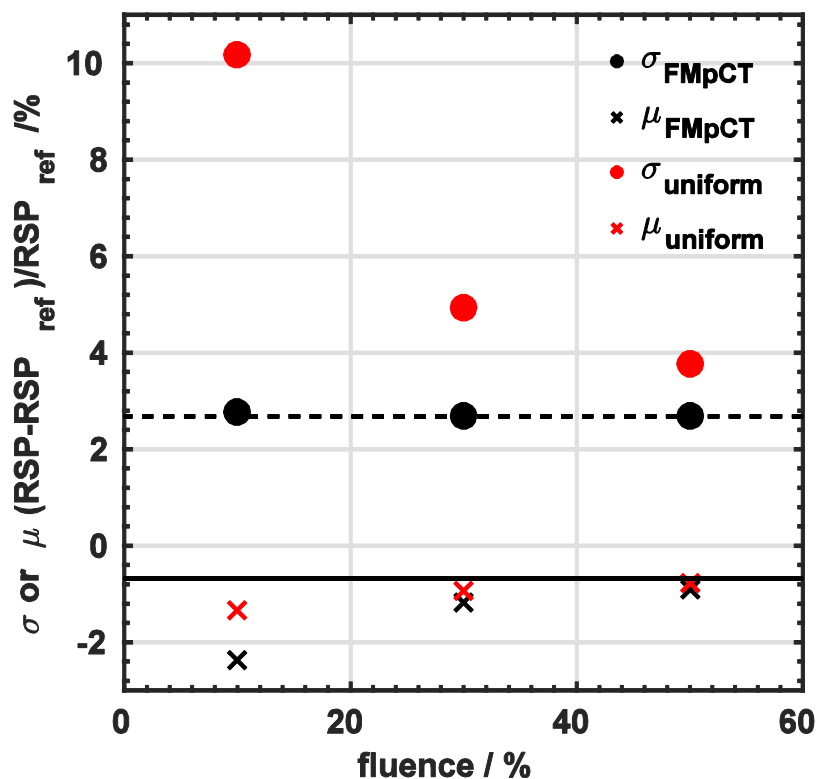
G. Dedes et al. FMpCT

Figure 14. Accuracy (mean, μ) and noise (1 standard deviation, σ) of FMpCT images (black data points) and uniform images (red data points) for various FMF (expressed as percentage of FF) in the ROI of the pediatric head phantom. The horizontal dashed (solid) line corresponds to the FF noise (accuracy).

5. Conclusion

In this work, we have applied the concept of fluence field modulation to proton CT, inspired by earlier work applied to x-ray CT. Using Monte Carlo simulations of an ideal proton CT scanner, we have confirmed that image quality could be varied across the proton CT image by modulating the proton fluence in a binary fashion. Our approach was successful for both homogeneous and anthropomorphic virtual phantoms, potentially allowing clinical imaging dose reductions ranging

from 37% to 56% outside the treatment area, while preserving full fluence image quality inside regions of interest. We additionally virtually implemented the method on broad beam proton CT experimental data and showed that fluence modulated proton CT should be realizable if proton pencil beam intensity and detector count rates can be adjusted to achieve the desired modulation levels. The concept of fluence modulation can be supplemented by energy modulation as well, as pCT imaging dose and noise levels are energy dependent, and we intend to investigate it as a continuation of the current study.

6. Acknowledgements

References

Agostinelli S, et al. 2003 Geant4-a Simulation Toolkit *Nucl Instrum Meth A* **506** 250-303

Arbor N, et al. 2015 Monte Carlo comparison of x-ray and proton CT for range calculations of proton therapy beams *Physics in medicine and biology* **60** 7585-99

Bartolac S, et al. 2011 Fluence field optimization for noise and dose objectives in CT *Medical physics* **38 Suppl 1** S2

Bartolac S and Jaffray D 2013 Compensator models for fluence field modulated computed tomography *Medical physics* **40** 121909

Brousmiche S, et al. 2015 TH-CD-BRA-04: Assessing How Stochastic CT Noise Can Lead to Systematic Proton Range Errors *Medical physics* **42** 3726-

Chvetsov A V and Paige S L 2010 The influence of CT image noise on proton range calculation in radiotherapy planning *Physics in medicine and biology* **55** N141-9

Cormack A M 1963 Representation of a Function by Its Line Integrals with Some Radiological Applications *J Appl Phys* **34** 2722-&

Farace P, et al. 2016 Pencil beam proton radiography using a multilayer ionization chamber *Physics in medicine and biology* **61** 4078-87

Giacometti V, et al. 2017 Software platform for simulation of a prototype proton CT scanner *Medical physics* **44** 1002-16

Graham S A, et al. 2007a Intensity-modulated fluence patterns for task-specific imaging in cone-beam CT *P Soc Photo-Opt Ins* **6510** U16-U24

Graham S A, et al. 2007b Compensators for dose and scatter management in cone-beam computed tomography *Medical physics* **34** 2691-703

Hansen D C, et al. 2014 The image quality of ion computed tomography at clinical imaging dose levels *Medical physics* **41** 111908

Hansen D C, et al. 2015 A simulation study on proton computed tomography (CT) stopping power accuracy using dual energy CT scans as benchmark *Acta oncologica* **54** 1638-42

Hansen D C, et al. 2016 Fast reconstruction of low dose proton CT by sinogram interpolation *Physics in medicine and biology* **61** 5868-82

Hudobivnik N, et al. 2016 Comparison of proton therapy treatment planning for head tumors with a pencil beam algorithm on dual and single energy CT images *Medical physics* **43** 495

Huesman R H, et al. 1975 Comparison of Heavy Charged Particles and x-Rays for Axial Tomographic Scanning *Technical Report*

Hünemohr N, et al. 2013 Ion range estimation by using dual energy computed tomography *Z Med Phys* **23** 300-13

Hünemohr N, et al. 2014 Experimental verification of ion stopping power prediction from dual energy CT data in tissue surrogates *Physics in medicine and biology* **59** 83-96

Hurley R F, et al. 2012 Water-equivalent path length calibration of a prototype proton CT scanner *Medical physics* **39** 2438-46

Johnson R P, et al. 2016 A Fast Experimental Scanner for Proton CT: Technical Performance and First Experience With Phantom Scans *Ieee T Nucl Sci* **63** 52-60

Kalender W A, et al. 2008 Technical approaches to the optimisation of CT *Physica medica : PM : an international journal devoted to the applications of physics to medicine and biology : official journal of the Italian Association of Biomedical Physics* **24** 71-9

Krah N, et al. 2015 An advanced image processing method to improve the spatial resolution of ion radiographies *Physics in medicine and biology* **60** 8525-47

Kurz C, et al. 2015 Comparing cone-beam CT intensity correction methods for dose recalculation in adaptive intensity-modulated photon and proton therapy for head and neck cancer *Acta oncologica* **54** 1651-7

Landry G, et al. 2015a Phantom based evaluation of CT to CBCT image registration for proton therapy dose recalculation *Physics in medicine and biology* **60** 595

Landry G, et al. 2015b Investigating CT to CBCT image registration for head and neck proton therapy as a tool for daily dose recalculation *Medical physics* **42** 1354-66

Lee J, et al. 2015 Sparse-view proton computed tomography using modulated proton beams *Medical physics* **42** 1129-37

Mail N, et al. 2009 The influence of bowtie filtration on cone-beam CT image quality *Medical physics* **36** 22-32

McCollough C H, et al. 2006 CT dose reduction and dose management tools: overview of available options *Radiographics : a review publication of the Radiological Society of North America, Inc* **26** 503-12

Mohler C, et al. 2016 Range prediction for tissue mixtures based on dual-energy CT *Physics in medicine and biology* **61** N268-75

Mulkens T H, et al. 2005 Use of an automatic exposure control mechanism for dose optimization in multi-detector row CT examinations: Clinical evaluation *Radiology* **237** 213-23

Murphy M J, et al. 2007 The management of imaging dose during image-guided radiotherapy: report of the AAPM Task Group 75 *Medical physics* **34** 4041-63

G. Dedes et al. FMpCT

Paganetti H 2012 Range uncertainties in proton therapy and the role of Monte Carlo simulations *Physics in medicine and biology* **57** R99-117

Park Y K, et al. 2015 Proton dose calculation on scatter-corrected CBCT image: Feasibility study for adaptive proton therapy *Medical physics* **42** 4449-59

Penfold S N, et al. 2009 A more accurate reconstruction system matrix for quantitative proton computed tomography *Medical physics* **36** 4511-8

Penfold S N, et al. 2010 Total variation superiorization schemes in proton computed tomography image reconstruction *Medical physics* **37** 5887-95

Quinones C T, et al. 2016 Filtered back-projection reconstruction for attenuation proton CT along most likely paths *Physics in medicine and biology* **61** 3258-78

Rinaldi I, et al. 2014 Experimental investigations on carbon ion scanning radiography using a range telescope *Physics in medicine and biology* **59** 3041-57

Rit S, et al. 2013 Filtered backprojection proton CT reconstruction along most likely paths *Medical physics* **40** 031103

Sadrozinski H F W, et al. 2016 Operation of the preclinical head scanner for proton CT *Nuclear Instruments and Methods in Physics Research Section A: Accelerators, Spectrometers, Detectors and Associated Equipment* **831** 394-9

Schmid S, et al. 2015 Monte Carlo study on the sensitivity of prompt gamma imaging to proton range variations due to interfractional changes in prostate cancer patients *Physics in medicine and biology* **60** 9329-47

Schneider W, et al. 2000 Correlation between CT numbers and tissue parameters needed for Monte Carlo simulations of clinical dose distributions *Physics in medicine and biology* **45** 459-78

Schulte R W, et al. 2005 Density resolution of proton computed tomography *Medical physics* **32** 1035-46

Schulte R W, et al. 2008 A maximum likelihood proton path formalism for application in proton computed tomography *Medical physics* **35** 4849-56

Shinoda H, et al. 2006 Application of heavy-ion CT *Physics in medicine and biology* **51** 4073-81

Stayman J W, et al. 2016 Fluence-Field Modulated X-ray CT using Multiple Aperture Devices *Proc Spie* **9783**

Szczykutowicz T P and Mistretta C A 2013a Design of a digital beam attenuation system for computed tomography. Part II. Performance study and initial results *Medical physics* **40** 021906

Szczykutowicz T P and Mistretta C A 2013b Design of a digital beam attenuation system for computed tomography: part I. System design and simulation framework *Medical physics* **40** 021905

Szczykutowicz T P and Mistretta C A 2014 Experimental realization of fluence field modulated CT using digital beam attenuation *Physics in medicine and biology* **59** 1305-26

Szczykutowicz T P, et al. 2015 Realization of fluence field modulated CT on a clinical TomoTherapy megavoltage CT system *Physics in medicine and biology* **60** 7245-57

Tanaka S, et al. 2016 Development of proton CT imaging system using plastic scintillator and CCD camera *Physics in medicine and biology* **61** 4156-67

Taylor J T, et al. 2016 An experimental demonstration of a new type of proton computed tomography using a novel silicon tracking detector *Medical physics* **43** 6129

Veiga C, et al. 2015 Cone-beam computed tomography and deformable registration-based "dose of the day" calculations for adaptive proton therapy *International Journal of Particle Therapy* **2** 404-14

Veiga C, et al. 2016 First Clinical Investigation of Cone Beam Computed Tomography and Deformable Registration for Adaptive Proton Therapy for Lung Cancer *International journal of radiation oncology, biology, physics* **95** 549-59

Yang M, et al. 2012 Comprehensive analysis of proton range uncertainties related to patient stopping-power-ratio estimation using the stoichiometric calibration *Physics in medicine and biology* **57** 4095-115